

# Hyperspectral Photoluminescence Imaging for Spatially Resolved Determination of Electrical Parameters of Laser-Patterned Perovskite Solar Cells

*Christof Schultz, Markus Fenske, Laura-Isabelle Dion-Bertrand, Guillaume Gélinas, Stéphane Marcet, Janardan Dagar, Andreas Bartelt, Rutger Schlatmann, Eva Unger, and Bert Stegemann\**

Absolute calibrated hyperspectral photoluminescence (PL) imaging is utilized to access, in a simple and fast way, the spatial distribution of relevant solar cell parameters such as quasi-Fermi level splitting, optical diode factor, Urbach energies  $E_u$ , and shunt resistances  $R_{sh}$ , without the need for electrical measurements. Since these metrics play a significant role in evaluating the process windows for electrical series interconnection by laser patterning, this approach is followed to systematically locate and quantify electrical losses that may occur as a result of the laser-patterning process for monolithic series interconnection. It is shown that both picosecond and nanosecond laser pulses can be used for successful series interconnection. In both cases, only minor lateral material alterations occur, localized in a few  $\mu\text{m}$  wide region adjacent to the edges of the scribe lines. Furthermore, the acquisition and analysis of these hyperspectral PL datasets provide insights in the material removal process, from which it is concluded that the perovskite is rather resilient against the thermal impact of the laser.

recycling, making them attractive for photovoltaic applications.<sup>[1,2]</sup> In recent years, laboratory-scale PSCs have experienced a huge increase in power conversion efficiency, reaching over 25%, which is in the range of crystalline Si-based solar cell efficiencies.<sup>[3]</sup> However, the efficiency of PSCs is decreasing from lab-scale sizes toward large-scale perovskite solar modules (PSMs) due to the challenging transferability of the processes and the decreasing quality of the perovskite films, which limits commercialization and thus practical PSC applications.<sup>[4]</sup>

One of these challenges in up-scaling PSCs and PSMs is the monolithic series-interconnection of the cells, which is inevitable for large areas and requires the development of reliable patterning processes.<sup>[5–8]</sup> The series interconnection is obtained by alternating layer deposition

## 1. Introduction

Organic–inorganic metal halide perovskites (MHPs) are promising light absorber materials for low-cost and high-efficiency solar cells. Perovskites solar cells (PSCs) offer outstanding optoelectronic properties such as a long charge-carrier lifetime and diffusion length, strong optical absorption ( $10^4$ – $10^5$   $\text{cm}^{-1}$ ), bandgap tunability over a broad spectral range ( $\approx 1.2$ – $3.0$  eV), very low defect density and high defect tolerance, low voltage losses, as well as photon

and laser-based patterning steps (P1, P2, and P3). While the P1 and P3 electrically separate the front and back contact layer of neighboring cells, respectively, the intermediate patterning step P2 locally opens the absorber and charge-transport layers and, thus, provides an electrical path between the back contact of one cell and the front contact of the neighboring cells. Pulsed lasers are the tool of choice for patterning the three scribe lines, due to their contactless application with a high reproducibility and precision. In earlier work, the general principles of

C. Schultz, M. Fenske, A. Bartelt, R. Schlatmann, B. Stegemann  
Faculty 1  
School of Engineering – Energy and Information  
HTW Berlin – University of Applied Sciences  
Wilhelmshofstr. 75a, D-12459 Berlin, Germany  
E-mail: bert.stegemann@htw-berlin.de

 The ORCID identification number(s) for the author(s) of this article can be found under <https://doi.org/10.1002/solr.202300538>.

© 2023 The Authors. Solar RRL published by Wiley-VCH GmbH. This is an open access article under the terms of the Creative Commons Attribution-NonCommercial-NoDerivs License, which permits use and distribution in any medium, provided the original work is properly cited, the use is non-commercial and no modifications or adaptations are made.

DOI: 10.1002/solr.202300538

L.-I. Dion-Bertrand, G. Gélinas, S. Marcet  
Photon etc  
5795 Av. de Gaspé, #222, Montréal, QC H2S 2X3, Canada

J. Dagar, E. Unger  
Young Investigator Group Hybrid Materials Formation and Upscaling  
Helmholtz-Zentrum Berlin für Materialien und Energie  
Kekuléstr. 5, D-12489 Berlin, Germany

R. Schlatmann  
Competence Centre Photovoltaics Berlin (PVcomB)  
Helmholtz-Zentrum Berlin für Materialien und Energie  
Schwarzschildstr. 3, D-12489 Berlin, Germany

laser patterning of thin films<sup>[9]</sup> and its application for monolithic series interconnection of PSM<sup>[5,8,10–12]</sup> were comprehensively described. There, it was demonstrated that, irrespective of the detailed configuration of the perovskite layer stack, the success of laser-based patterning is based on precisely controlled energy input. Since the aim is always to produce well-defined scribe lines without unintended material modifications due to excess laser energy, patterning of MHP remains challenging due to the pronounced thermal sensitivity of the perovskite material itself and the inevitable introduction of excess laser energy, in particular at the pulse-to-pulse overlap regions or at the scribe-line edges. In both cases, the introduced excess energy can easily cause material alterations, forming electronic defects which might result in nonoptimal electrical functionality, as shown in our recent work.<sup>[6,13]</sup>

To meet these challenges, a versatile, nondestructive, easy-to-use, and fast method for evaluating the patterning process is needed to quantify the lateral distribution of key solar cell parameters, which is increasingly important for successful process control in laser patterning and optimizing the device performance. Photoluminescence measurements have been proven as versatile method to access material properties<sup>[14–16]</sup> for decades. It has been applied to derive the optoelectronic material properties and can be utilized to get insights into defect-related charge-carrier recombination.<sup>[16–19]</sup> In recent years, spectrally resolved photoluminescence (PL) imaging has been implemented in high-resolution microscopes, now enabling a rapid analysis of solar cells and modules. This technique, called hyperspectral PL imaging, combines the established PL imaging and spectrally resolved measurement technique in one method which has evolved to a key nondestructive measurement.<sup>[20]</sup> Based on such measurements, pristine perovskite layers have been investigated in the past and mathematical calculations have been established, enabling the derivation of various material as well as important solar cell parameters. In the present study, we performed absolute-calibrated hyperspectral PL imaging at inhomogeneous perovskite layers, i.e., perovskites which have been patterned by laser, and applied these methods, to identify undesired effects of laser scribing on the MHP layer and to be able to draw conclusions on the influence of the patterning process on the material behavior at the scribe-line edges and bottoms. While in the conventional approach, PL imaging is typically applied to characterize solar cells, focusing on the detection of spatial intensity variations to assign them, e.g., to local variations in sample composition,<sup>[15,21,22]</sup> we show that hyperspectral PL imaging adds a huge benefit when applied to laser patterned samples since several opto-electronic material properties, such as quasi-Fermi level splitting (QFLS),<sup>[16,17]</sup> the Urbach energies ( $E_u$ ),<sup>[23,24]</sup> the PL quantum yield (PLQY),<sup>[17]</sup> the optical diode factor (ODF),<sup>[25–28]</sup> the PL central emission wavelength, and the shunt resistances  $R_{sh}$ <sup>[29]</sup> can be easily derived. This provides direct information about the opto-electronic material properties in the vicinity of the laser-scribed lines and greatly facilitates the determination of suitable process windows to optimize for laser patterning.

For these studies, the P3 scribe line from complete PSCs is investigated. In principle, two designs are common for the P3, either only the back contact is patterned or, more commonly, both the back contact and the absorber layer are patterned (as shown in **Figure 1**). We decided for the latter option, but

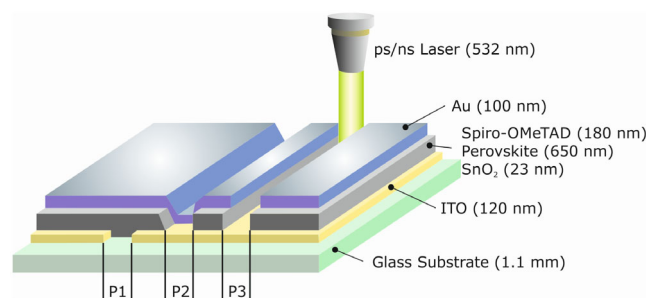


**Figure 1.** Schematic illustration of the utilized sample layer stack and the laser-based monolithic series interconnection with the three patterning steps P1, P2, and P3.

ensured that the removal of the perovskite absorber layer did not damage the underlying TCO contact in any way, preferring to leave some residual perovskite in the trench, which does not affect the electrical isolation between the neighboring cells. After P3 patterning, the metal back-contact layer was then removed to allow PL measurements to be performed on the perovskite layer.

To investigate the different influence of the laser pulse length, P3 patterning was performed with both nanosecond and picosecond laser pulses at laser fluences that are within the optimal process windows determined previously.<sup>[6,13]</sup> The P3 patterning process was chosen because it is of particular importance for the cell efficiency. It separates neighboring cells by cutting through the back contact and the perovskite absorber layer down to the front contact layer whereby excess energy easily can modify the perovskite and cause electrical power losses, which is less critical in the P2 or P1 step.

In the following, the mathematical approach for the quantitative determination of the material and solar cell parameters listed earlier is presented and directly applied to the P3 laser patterned PSCs. The underlying measured data were acquired by means of global hyperspectral PL using two different excitation wavelengths (405 and 532 nm). Using this approach, we show that these metrics can be utilized to investigate the effects of laser patterning itself on the pristine layer stack. This is followed by a discussion on the qualitative evaluation of the influence of the lasers pulse length on the material properties in the context of determining the optimum patterning process window.

## 2. Experimental Section

### 2.1. Sample Preparation

The sample preparation processes followed the procedure for perovskite baseline samples described in detail in refs. [5,30] resulting in the layer stack schematically depicted in **Figure 1** and is summarized as follows: Standard inch-size glass substrates were coated with 120 nm indium tin oxide (ITO,  $R_{sheet} \approx 15 \Omega \square^{-1}$ ). The ITO front contact was laser patterned (P1) to establish a monolithic series interconnection, as also shown in **Figure 1**. This step defines the width of the resulting cell stripes and electrically separates the individual cells from each other. All samples were then cleaned in an ultrasonic bath (900 s each in a soap solution of deionized water and acetone and

in isopropanol), dried with N<sub>2</sub>, and then treated with UV–ozone for 900 s. A tin-oxide (SnO<sub>2</sub>) solution was set by dissolving SnCl<sub>2</sub>·2H<sub>2</sub>O in ethanol and stirring for 12 h at room temperature and subsequently deposited by spin-coating to form the SnO<sub>2</sub> electron-transport layer (ETL). The spinning speed was first set at 1500 rpm for 30 s and then increased to 2500 rpm for an additional 30 s. Finally, the ETL was cured in ambient atmosphere at 180 °C.<sup>[30]</sup> Then, the triple-cation perovskite solution Cs<sub>0.05</sub>FA<sub>0.79</sub>MA<sub>0.16</sub>PbBr<sub>0.51</sub>I<sub>2.49</sub> was deposited also by spin-coating.<sup>[30,31]</sup> Next, the hole-transport layer (HTL) was deposited by dissolving a 36.2 mg mL<sup>-1</sup> concentration of spiro-OMeTAD precursor in chlorobenzene, doped with 4-tert-butylpyridine (TBP, 14.4 μl mL<sup>-1</sup>), Li-TFSI (8.8 μl mL<sup>-1</sup>), and cobalt(III) complex (14.5 μl mL<sup>-1</sup>) dopants. The spiro-OMeTAD solution was spin-coated over the perovskite film at a spinning speed of 1800 rpm for 30 s.<sup>[32]</sup> To enable an electrical connection to the subsequently deposited back contact, a path was created through the perovskite absorber layer by laser patterning (P2 patterning step). The back-contact layer was formed by evaporation of gold under a low pressure. Its final thickness was about 100 nm. The third patterning step (P3) electrically separated the back-contact layer. Note: All the materials utilized in this work (see Table 1) were directly used for device fabrication without further modification, such as dilution.

## 2.2. Laser Patterning

The patterning of the perovskite samples was carried out by using a commercially available, customized laser system (Rofin Baasel Lasertech). This system was equipped with a nanosecond (ns) laser source (SL3PV) and a picosecond (ps) laser source (Time Bandwidth, Duetto), both emitting laser pulses with a wavelength of 532 nm and pulse durations of about 20 ns and 10 ps, respectively. The maximum pulse energy of

the ns laser was about 32 μJ at 20 kHz, and a maximum pulse energy of 48 μJ at 100 kHz was available for the ps laser. The laser beam diameters 2ω<sub>0</sub> at the focal position were determined according to the method of Liu,<sup>[33]</sup> leading to values of 28.1 μm ± 10% for the ns laser and 26.7 μm ± 10% the ps laser. The laser system is equipped with fixed optics to guide the laser beam to the sample surface and an x–y motion system to translate the samples with speeds up to 1.2 m s<sup>-1</sup>, while maintaining a positioning accuracy below 5 μm for each stage. To avoid material degradation and to collect dust and debris resulting from the ablation process, the samples were patterned in a closed chamber with a continuous nitrogen flow.

P3 patterning was performed with both ns and ps laser pulses in such a way that both the metallic back contact and the perovskite layer were patterned. The applied patterning parameters were elaborated in a previous study and can be found there in detail.<sup>[6]</sup> Following this previous study, the P3 scribe lines were patterned multiple times (3×) without any lateral displacement to achieve sufficient electrical isolation of neighboring cells while maintaining a narrow interconnection width. The optimal process windows for P3 patterning have been previously determined based on morphological chemical and electrical analyses. Accordingly, laser fluences of about 2.31 and 1.16 J cm<sup>-2</sup> were used here for ns and the ps laser patterning, respectively. Both values are within the respective optimal process windows. The overlap between subsequently patterned pulses was about 12% for a single pass.

## 2.3. Characterization Techniques

The PL global measurements were performed with a commercially available hyperspectral imaging system (IMA, Photon, etc.).<sup>[20]</sup> Two continuous wave lasers with wavelengths of 405 and 532 nm were used to excite the sample. The laser excitation source was spread homogeneously over the entire field of view allowing global imaging. The incident photon flux could be adjusted and was set to 86 mW cm<sup>-2</sup> for each laser of the measurements presented here. Images were acquired with a microscopy objective (20×) with the PL directed onto a Si CCD camera via a volume Bragg grating at room temperature. The spatial resolution was close to the diffraction limit and was around 1 μm and the spectral resolution better than 2.5 nm. The schematic representation of the data acquisition procedure, that basically includes: 1) data acquisition, 2) wavelength rectification, 3) photometric calibration and background removal, and 4) quantitative data analysis, is given in Figure 2.

## 3. Determination of Material and Solar Cell Parameters

### 3.1. Background and Data Acquisition

Several previous studies have demonstrated the applicability of PL imaging for material characterization in photovoltaics, even for thin-film materials such as CIGSe and perovskites.<sup>[16,17,21,34,35]</sup> Several methods for deriving electronic and optoelectronic properties and determining the parameters listed previously have been established, calculating the metrics usually

**Table 1.** Materials and solutions used for PSM fabrication.

Materials	Supplier
Formamidinium iodide (FAI)	Dynamo
Methylammonium bromide (MABr)	Dynamo
4-tert-butylpyridine (TBP)	Dynamo
Cobalt (III) complex	Dynamo
Indium-tin-oxide-covered glass substrates	Lumtec
Spirobifluorene (spiro-OMeTAD) (≥99.8%)	Merck
Tin chloride (SnCl <sub>2</sub> ·2H <sub>2</sub> O) dehydrate	Sigma-Aldrich
Dimethyl sulfoxide anhydrous (DMSO, ≥ 99.9%)	Sigma-Aldrich
N,N-Dimethylformamide anhydrous (DMF, 99.8%)	Sigma-Aldrich
Chlorobenzene	Sigma-Aldrich
Ethanol (99.8%)	Sigma-Aldrich
Cesium iodide (CsI)	Sigma-Aldrich
Li-bis (trifluoromethanesulfonyl)imide (Li-TFSI)	Sigma-Aldrich
Tin chloride dihydrate (SnCl <sub>2</sub> ·2H <sub>2</sub> O)	Sigma-Aldrich
Lead (II) iodide (99.99%, trace metals basis)	TCI Deutschland GmbH
Lead bromide (PbBr <sub>2</sub> )	TCI Deutschland GmbH

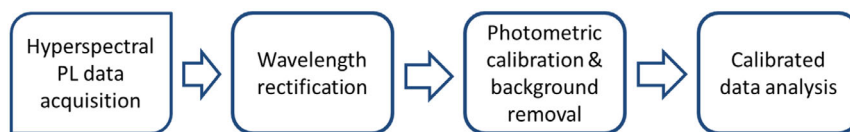


**Figure 2.** Simplified procedure of the hyperspectral photoluminescence (PL) data acquisition and subsequent treatment for quantitative analysis.

from a single image; only the calculation of the ODF requires PL measurements recorded at different, but known, excitation intensities. In this work, we will focus on the calculation of the QFLS, the PL peak shift, the Urbach energy, the PLQY, ODF, and  $R_{sh}$  as these quantities effectively represent the impact of the laser fluence on the electrical performance of the scribe-line surrounding material (e.g., carrier-trapping and charge-carrier extraction) and thus of the series-interconnected solar cells. In our recent work, we have shown that the impact of the laser scribing on the perovskite material is confined to a narrow range aside the scribe line.<sup>[13]</sup> Thus, by imaging a sufficiently large range aside from the laser scribe, the remotely located and thus putatively unaffected material can be used as reference for comparison with the directly affected material located close to the scribed line. In this way, the success of the patterning process itself can be qualitatively evaluated. To accomplish this purpose, the following step-by-step procedure describes how to derive first the QFLS and then the related parameters, as listed before, from the acquired hyperspectral PL datasets.

First, the PL images must be noise-corrected (dark noise of the camera chip) as part of the data acquisition and it must be ensured that the recorded images contain all emitted photons of a certain wavelength interval—either by using an integrating sphere or by computational correction. The image size should ideally cover a lateral area in the range of the laser scribe-line width ( $\approx 50 \mu\text{m}$ ) to use distant areas as reference where no thermal impact from, introduced by the laser scribing, would be expected. In the case of ns laser pulses, the thermal diffusion length can be calculated by using an established formula,<sup>[36]</sup> in PSC the approximated length is in the range of  $1 \mu\text{m}$ . Thus, a lateral spacing of about the laser scribe-line width is sufficient to use remote areas as reference.

### 3.2. Calculation of the QFLS

The QFLS  $\Delta\mu$  refers to the splitting of the quasi Fermi levels at the electron and the hole contacts under illumination. Typically, the effective QFLS ( $\Delta\mu_{\text{eff}}$ ) is measured since the illuminated sample area is not infinitely small and extends over larger areas with several grain boundaries. These internal interfaces cause internal losses reducing the ideal QFLS. The PL emission  $\Phi_{\text{PL}}$  of the solar cells at thermal equilibrium and at room temperature can be described by the generalized Planck's law using the Boltzmann approximation for a black body.<sup>[16,37]</sup> Since the solar cell is not an ideal black body, the samples absorptance  $A(E)$ , i.e., the ratio of absorbed photons to the number of incident photons or the absorption probability, has to be considered.<sup>[16]</sup> The emission of photons into the hemisphere  $\Omega$  above the sample surface (at room temperature and under illumination) can be approximated by Equation (1)<sup>[16,37]</sup>

$$\phi_{\text{PL}} \approx A(E) \frac{\Omega E^2}{4\pi^3 \hbar^3 c^2} \frac{1}{e^{\left(\frac{E - \Delta\mu_{\text{eff}}}{kT}\right)}} \quad (1)$$

The reduced Planck constant is represented by  $\hbar$ ,  $c$  is the speed of light within the considered material,  $E$  is the energy of the considered wavelength, and  $kT$  is the thermal energy. The effective angle of photon emission is typically smaller than a full hemisphere. Only photons, emitted under an angle below the critical angle, are able to exit the perovskite sample surface, while at higher angles total internal reflection occurs. To account for this behavior,  $\Omega$  can be approximated by  $\pi/n_2^2$  ( $n_2 =$  refractive index of the photon-emitting material) and  $c$  can be replaced by  $c_0$ , the speed of light in vacuum.<sup>[16]</sup>

Before the calculation of the local QFLS can be carried out, the central wavelength (PL peak position) of the PL emission spectrum must first be determined, since this central wavelength corresponds to the distinct energy of the optical bandgap of the semiconductor material and the majority of the photons are emitted from the material via this transition. Thus, the QFLS is assigned to this central wavelength.

To detect shifts of the central wavelength in the scribed lines or in the edge areas of the lines, the local central wavelength, derived from pixel-by-pixel analysis of the PL spectra, at which the PL emission maximum occurs was determined in each case. The results of the determination of the central wavelength is provided in **Figure 3** (upper row), showing two images of scribe lines patterned with (A) ns and (B) ps pulses with optimum fluences and the respective optimal fluences determined previously.<sup>[6,13]</sup> In both cases, the central PL wavelength next to and within the scribe lines is in a narrow range of  $758 \text{ nm} \pm 3 \text{ nm}$ , corresponding to an optical bandgap energy of about  $1.64 \text{ eV}$ . A typical example of the spectrally resolved PL curve with a maximum at  $758 \text{ nm}$  is given in Figure S1, Supporting Information. The low-intensity signal inside the laser-scribed trench originates from small amounts of residual perovskite, that apparently remained in the trench, thus ensuring that the underlying TCO layer was not damaged during laser patterning.

However, the images indicate a pronounced redshift of the central wavelength at the inner scribe-line edges, up to a few tens of nm, which is accompanied by small dots distributed over the sample surface. The shift of the central wavelength at the inner edges can be attributed to strong material degradation during the patterning process itself. For the scribe-line characterization, however, the inner edges play a rather minor role. Interestingly, the small redshifted dots spread over the sample surface allow conclusions to be drawn about the material removal process. Obviously, critical heating and explosive boiling occurs, producing splashes that condense incongruently and are widely distributed over the sample surface. This hypothesis has been established in our previous studies and simulations of the

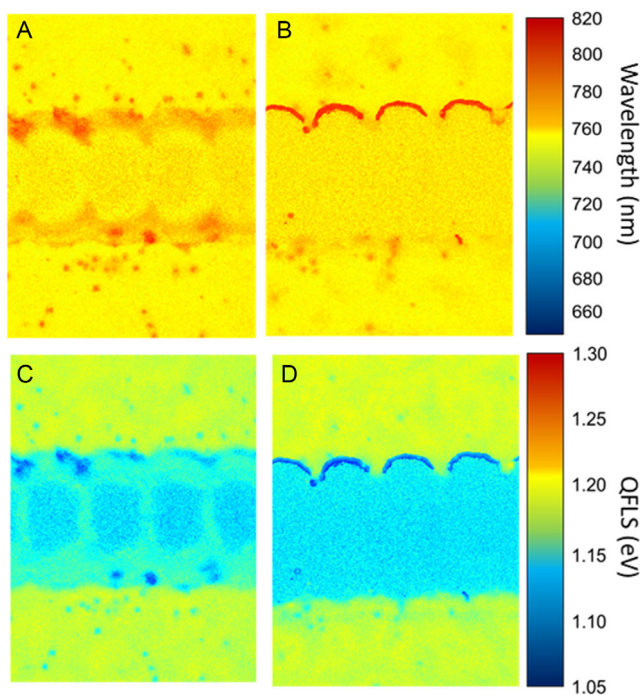


**Figure 3.** A,B) Spatially resolved images of the local central wavelength of PL emission and C,D) the corresponding quasi-Fermi level splitting (QFLS). The samples were patterned by (A,C) ns and (B,D) ps laser pulses at optimum fluences of 1.36 and 2.31 J cm<sup>-2</sup>, respectively.

ablation process, see refs. [5,38], and is further supported by the scanning electron microscopy and energy-dispersive X-ray spectroscopy images shown in Figure S2, Supporting Information, which reveals an accumulation of iodine at these dots. This effect will be addressed in more detail in a subsequent paper. However, it can be stated here that the occurrence of debris in the vicinity of the scribe lines may generally negatively influence the subsequent layer deposition steps. Thus, it is also a measure for the characterization of the laser scribe lines and can be used to qualitatively evaluate the patterning process.

It should be noted that the different appearance of the scribe-line edges is due to deviations from the ideal Gaussian intensity distribution, which affects the laser beam shape at the focal position. This somewhat reduced beam quality is related to an already slightly degraded laser crystal, which can occur with frequent and continued use in practice. Ideally, the beam would be perfectly circular. However, the nonideal intensity distribution is not expected to affect the active zone noticeably, since the scribe-line edges indicate a shift in the central wavelength only in a very narrow range, i.e., much less than half a scribe-line width.

Once the central wavelength has been determined, Equation (1) can be rearranged to determine the effective QFLS  $\Delta\mu_{\text{eff}}$  for each pixel in the recorded hyperspectral PL dataset. At open-circuit condition and without any internal losses, or by neglecting additional internal losses, the effective QFLS can be directly converted to the externally accessible open-circuit voltage ( $V_{\text{oc}} = \Delta\mu_{\text{eff}}/q$ ;  $q$  is the elemental charge), which is one of the most important parameters for the electrical solar cell performance. In Figure 3 (lower part), the derived effective QFLS is

shown for ns (C) and ps (D) laser patterning, respectively. In both cases, the QFLS in the regions unaffected by the laser is about 1.19 eV, which is below the intensity maximum of the PL observed at 1.64 eV (cf. Figure 3A,B and S1, Supporting Information) and can be assigned to interfacial recombination processes.<sup>[39]</sup> The images show in both cases, i.e., ns and ps laser patterning, an abrupt decrease in the calculated QFLS at the scribe-line edges by up to 60 meV and slighter fluctuations in the vicinity of the scribe lines. The positions of the abrupt change of  $\Delta\mu_{\text{eff}}$  coincide exactly with the positions where the central wavelength of the PL emission is shifted to higher wavelengths corresponding to lower energies. Moreover, the abrupt change of the QFLS at the outer scribe-line edges indicates that the perovskite material has not been altered by the patterning process beyond the previously approximated thermal diffusion length. From the analysis of the QFLS images, it can be concluded that the application of both ns and ps laser pulses at optimum fluence does not cause thermally induced modifications, confirming the interpretations of previous works.<sup>[13]</sup>

### 3.3. Calculation of the Urbach Energy

The Urbach energy  $E_u$  expresses the temperature-dependent onset sharpness of absorption in highly ordered, crystalline semiconductors.<sup>[40,41]</sup> It is a measure of the sum of static disorder (i.e., due to grain boundaries or compositional differences causing bandgap fluctuations) and dynamic disorder caused by thermal effects.<sup>[16,42]</sup> In general, the Urbach energy is related to the density of state distribution near the band edges and is therefore commonly used as an indicator of the electronic quality of thin films used as absorbers in solar cells.<sup>[40,42–44]</sup> Thus, determining the Urbach energy is a useful tool to identify and address material-related issues that may affect device performance. A lower  $E_u$  typically indicates a lower concentration of defects or trap states within the material, which corresponds to a higher material quality that is crucial for efficient solar cell performance. In addition, a lower  $E_u$  also implies a sharper absorption edge, meaning that more of the incident solar spectrum can be efficiently absorbed. This is important for maximizing the photocurrent generation in solar cells. Since the Urbach energy can also influence the charge-carrier transport, a lower  $E_u$  is generally associated with a longer carrier diffusion length and more efficient carrier transport, leading to higher solar cell performance.

For disordered materials such as organic or semi-organic solids, which include PSCs, the applicability and significance of the Urbach energy is still under discussion.<sup>[40,44]</sup> Nevertheless, it has been shown also for PSC that the empirical correlation between low Urbach energies and the open-circuit voltage deficit holds.<sup>[41–43]</sup> Thus,  $E_u$  can be directly interpreted as measure of the local solar cell performance, since it provides information about material quality, defect states, non-radiative recombination, and the efficiency of light absorption. With regard to the characterization of the laser-scribed lines, it is thus a sensitive measure to reveal laser-induced material alterations.

In thermodynamic equilibrium, the emissivity and the absorptivity of a given body are in equilibrium, i.e.,  $\phi_{\text{PL}}(E) \propto A_{\text{PL}}(E)$ , as stated by Kirchhoff's law of thermal radiation. This law also

applies to the emitting ( $\phi_{PL}$ ) and absorbing ( $A_{PL}$ ) spectra which directly show the absorption and emission behavior around the optical bandgap. Under these assumptions, the Urbach energy can be extracted from the PL spectrum, by determining the inverse low energy slope of the logarithm of the PL spectrum plotted against the emission energy, according to Equation (2)<sup>[16,42]</sup>

$$E_U = \left( \frac{\Delta \ln(\phi_{PL})}{\Delta E} \right)^{-1} \quad (2)$$

This procedure was applied to each pixel and resulted in the Urbach energy mapping. In **Figure 4**, the calculated Urbach energy mappings, for the ns (A) and ps (B) laser-patterned samples, are shown. The images show a rather homogenous level of the Urbach energies in the scribe-line vicinity and for remote area of a value of about 30 meV. Higher values of about 45 meV can be seen directly at the inner scribe-line edges. Here, too, an abrupt change in the calculated Urbach energies can be found, which is well pronounced for ps laser pulses (B) and slightly less pronounced for the utilization of ns laser pulses (A). Additionally, it is striking that the broadly scattered splashes, seen in the central wavelength images (Figure 3A,B), cannot be observed here and thus do not appear to play a role in the Urbach energy. The enhanced Urbach energies at the inner scribe-line edges indicate deep tail-states causing the observed redshift of the central wavelength and fit also well with lowered QFLS which was observed in Figure 3. With regard to the characterization of the laser scribe, it can be concluded that the lowered Urbach energies at the scribe-line edges can be, as already stated before, assigned to residues or debris as a result of the patterning process itself. The analyses of the outer scribe-line edges do not show a significant difference in the calculated Urbach energies. Thus, it can be concluded that both ns and ps pulses are well-suited for laser patterning since they do not cause detectable material modification.

### 3.4. Calculation of the PLQY

PLQY measurements are valuable for assessing the efficiency of light emission in perovskite materials and understanding the

impact of defects or processing conditions on the luminescence properties and thus power generation in PSCs. The PLQY is the ratio between the number of emitted photons ( $\phi_{em}$ ) and the number of absorbed photons ( $\phi_{ab}$ ). Under open-circuit conditions, the external charge extraction is zero. Thus, the PLQY represents the ratio of radiative recombination ( $\phi_{rad}$ ) to the sum of the radiative and non-radiative recombination ( $\phi_{n-rad}$ ), as expressed by Equation (3).

$$PLQY = \frac{\phi_{em}}{\phi_{ab}} = \frac{\phi_{PL}}{\phi_L \times R} = \frac{\phi_{rd}}{\phi_{rd} + \phi_{n-rad}} \quad (3)$$

The number of emitted photons ( $\phi_{PL}$ ) is directly measured with the absolute calibrated hyperspectral setup. The number of incident photons can be derived from the laser power, which must be converted into the number of emitted photons with regard to their specific photon energy ( $\phi_L$ ). Only the degree of reflectance ( $R$ ) needs to be known, it can be derived from UV-vis spectroscopy measurements. In our case, the reflectance is estimated to be 5%. A further aspect is the possible photon recycling. Since our investigated PSCs have a relatively long charge-carrier lifetime and diffusion length, photon recycling could occur and have a significant impact on the internal luminescence conditions<sup>[45,46]</sup> and thus on the electronic material properties. Nevertheless, we assume that the relative change of the PLQY is sufficient to evaluate the laser-patterning processes.

Generally, a high QFLS indicates efficient charge-carrier separation and a high potential difference for electron and hole transport. This often leads to a high PLQY because photogenerated electron-hole pairs are more likely to recombine radiatively, implying that a significant portion of the absorbed light is converted into luminescence and potentially into electrical current. However, the relationship between QFLS and PLQY can be influenced by factors such as defects or compositional alterations of the material, that both quantities are possibly not directly correlated anymore.

Based on Equation (3), the PLQY images were calculated for the case of ns and ps laser pulses with optimum fluence and are shown in **Figure 5**. Three interesting features can be observed there. First, when comparing the inner edges of the laser scribe lines, a distinct region with remarkable lowered PLQY

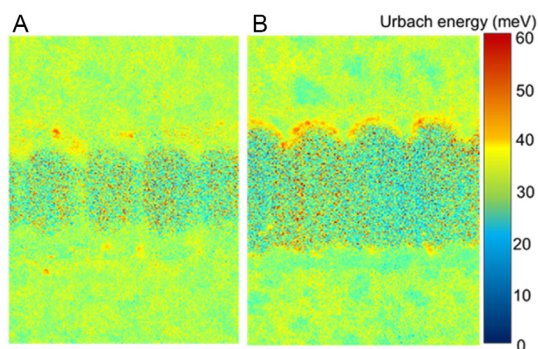


**Figure 4.** Spatially resolved images of the Urbach energy for the case of laser patterning by A) ns and B) ps laser pulses at optimum fluences of 1.36 and 2.31 J cm<sup>-2</sup>, respectively.

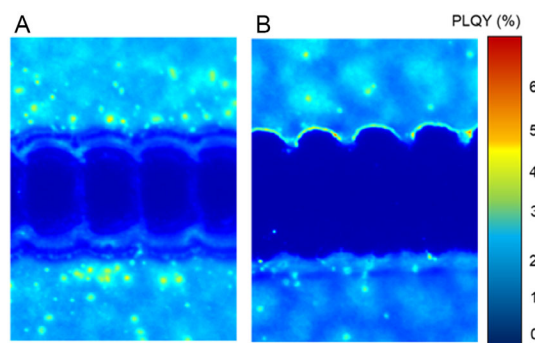


**Figure 5.** Spatially resolved images of the PL quantum yield for the case of laser patterning by A) ns and B) ps laser pulses at optimum fluences of 1.36 and 2.31 J cm<sup>-2</sup>, respectively.

(compared to the PLQY observable at remote positions) can be identified in the case of ns laser pulses (A), which is not observed for ps laser pulses (B). Second, the number of broadly scattered dots adjacent to the laser scribe line is significantly higher for ns laser pulses and third, their PLQY is higher than the PLQY in distant region. The latter could be the result of either iodide-rich debris, acting as sink and collecting charge carriers. Another explanation could be the absence of charge-transport layers, enabling a higher lifetime at these sites. However, neither explanation is entirely satisfactory, since debris is considered a disordered residue with rather poor radiative efficiency and the delamination of the charge-carrier-transport layer from the perovskite does not seem very likely. The origin of the behavior remains unclear and further investigations are needed to clarify this. More important is the difference at the inner scribe-line edges. With regard to Equation (3), the lower PLQY observed for ns laser pulses can be attributed to a higher degree of non-radiative recombination, presumably caused by the thermal treatment of the material by the laser pulse. These results are in good agreement with the previous analyses of the QFLS and underline that the application of ps laser pulses is more efficient with regard to the amount of removed material and introduces less modifications.

### 3.5. Calculation of the ODF

Originally, the diode factor of a solar cell is derived from electrical measurements of the current density–voltage ( $J$ – $V$ ) behavior, which is affected by the recombination processes that occur.<sup>[16,25–27]</sup> It is a sensitive measure of the electron capture and release processes that cause a shift in QFLS<sup>[26]</sup>. The lower the non-radiative recombination, the lower the QFLS, which is also expressed in a low value of the diode factor. Since the QFLS is related to the  $V_{oc}$  and thus to the fill factor, a low diode factor is desirable. Recently, it has been shown that intensity-dependent PL measurements can be used to determine a very similar parameter, namely the ODF. The ODF can be derived from the slope of the logarithmically plotted PL intensity ( $\phi_{PL}$ ) as a function of the logarithmically plotted excitation intensity ( $\phi_L$ ), as described by Equation (4).

$$\phi_{PL} \sim \phi_L \rightarrow \text{ODF} = \frac{\Delta \ln(\phi_{PL})}{\Delta \ln(\phi_L)} \quad (4)$$

The detailed derivation of how the ODF can be determined, which assumptions must be made, and why both the diode factor and the ODF are equivalent for complete devices is explained elsewhere.<sup>[25,26,47]</sup> However, the ODF represents the change in luminescence behavior as a function of the excitation intensity. Ideally, the proportionality is 1 for solely band–band recombination, while higher values indicate additional internal non-radiative processes such as competing recombination processes.<sup>[25,26]</sup> In real devices, however, the ODF is rarely 1. Usually this value is slightly higher. To utilize this parameter for scribe-line evaluation, its relative change in the vicinity of the scribe line is a sufficiently accurate measure.

Typically, the ODF is derived from measurements recorded with different excitation intensities at the same wavelength. In our case, the samples were excited successively with two different

lasers at 405 and 532 nm, each with an intensity of about  $86 \text{ mW cm}^{-2}$  (0.86 sun equivalents). The difference in the numbers of photons then results from the difference in the energy of the excitation photons. Thus, the difference in the charge-carrier generation behavior must be considered, which was realized by correcting the measured PL intensity by the spectral sensitivity (spectral response) from external quantum efficiency measurements. Accordingly, **Figure 6** shows the calculated ODF for samples patterned with ns (A) and ps pulses (B) at optimum laser fluence.

The ODF calculated from the images in Figure 6 reveals a range between 2.0 and 2.5 for both the ns and ps laser-patterned samples, which is notably higher than the ideal case. Moreover, the calculated ODF varies considerably aside the laser scribe lines and some of the broad spread splashes even show higher values up to 4. Additionally, in the case of ns laser pulses, the inner scribe edge shows a narrow region with a very low ODF. Interestingly, only some of the spread splashes exhibit higher ODF values, whereas some others show a behavior similar to the untreated perovskite material. These observations cannot be clearly explained by physical processes, so further investigations are needed to clarify this behavior. However, with regard to the evaluation of the laser-scribing processes, it can be stated that no material modifications in the vicinity of the scribe lines can be observed which is in good agreement to the previous results.

### 3.6. Calculation of the Local Shunt Resistance

The local shunt resistance ( $R_{sh}$ ) is a measure of the solar cell that correlates with the charge-carrier dynamics, i.e., current leakage, which in turns can be utilized to qualify the laser-scribing process. Originally, the method for calculating the local shunt resistance was introduced by Augarten et al.<sup>[29]</sup> In this work, we use an adapted approach, based on his “global method”, and described in the following by Equation (5).

$$R_{sh} = \frac{dV}{dI} = \frac{\Delta \mu_{eff}}{J_{sc} \times \left(1 - \frac{\phi_{pixel}}{\phi_{max}}\right)} \quad (5)$$

Thus, for the calculation of the local shunt resistance, the values of the local voltage and the local current are required. The

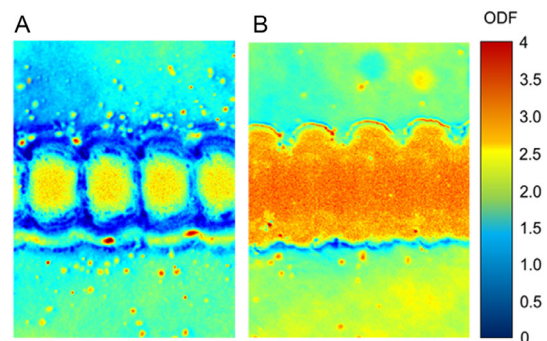


**Figure 6.** Spatially resolved images of the local optical diode factor (ODF) for the case of laser patterning by A) ns and B) ps laser pulses at optimum fluence of  $1.36$  and  $2.31 \text{ J cm}^{-2}$ , respectively.

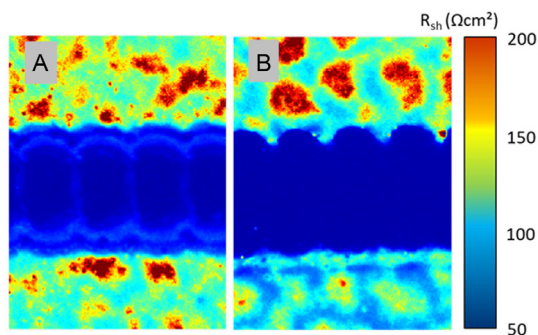


**Figure 7.** Spatially resolved images of the local shunt resistance for the case of laser patterning by A) ns and B) ps laser pulses at optimum fluences of 1.36 and 2.31 J cm<sup>-2</sup>, respectively.

local voltage is provided pixelwise by the previously calculated effective QFLS ( $\Delta\mu_{\text{eff}}$ ). At a localized shunt position, the emitted PL intensity is decreased compared to unaffected, pristine material. Thus, the short-circuit current is scaled proportionally to the PL intensity drop between the pristine and “perfect” material and the material in the vicinity of localized defects. It is assumed that the number of emitted photons is proportional to the number of excess charge carriers and that each photon generates one electron.<sup>[48]</sup> Then, the local current is given by the quotient of the PL emission of the corresponding pixel ( $\phi_{\text{pixel}}$ ) divided by the maximum value of the PL emission for pristine material ( $\phi_{\text{max}}$ ) subtracted from the short-circuit current. In our case, the short-circuit current density was about 22 mA cm<sup>-2</sup> derived separately from  $J$ - $V$  measurements. It should be noted that for inhomogeneously emitting samples the calculated  $R_{\text{sh}}$  value is strongly affected by these PL fluctuations. Therefore, the absolute value of  $R_{\text{sh}}$  has to be considered with caution whereas relative changes still clearly indicate material modifications due to the laser-scribing process. **Figure 7** shows the calculated shunt resistance images for the scribe lines patterned by ns (A) and ps (B) laser pulses with optimum fluences of 2.31 and 1.36 J cm<sup>-2</sup>, respectively.

There, the images show clearly pronounced regions with strongly changing shunt resistances. Additionally, in both cases, a rather homogenous level of the calculated resistance can be observed within the scribe lines and an abrupt change of the  $R_{\text{sh}}$  is found at the scribe-lines edges. The abrupt change in the  $R_{\text{sh}}$  at the scribe-line edges is very similar for both applied lasers. Interestingly, the “islands” aside the scribe lines have a strong influence on the calculated  $R_{\text{sh}}$ , which has been observed in previous images (c.f. Figure 5). The latter are assumed to originate from local material inhomogeneities, presumably bromide-rich and iodide-rich regions, which might indicate the onset of material degradation.<sup>[6,49]</sup> A frequency distribution of the calculated shunt resistance values is displayed in Figure S3, Supporting Information. As a result of the  $R_{\text{sh}}$  analysis, no significant differences in the calculated  $R_{\text{sh}}$  were found indicating an equally good suitability of both laser pulse durations. Thus, it can be concluded that both methods enable sufficient scribe-line properties without introducing lateral material modifications that up in an altered  $R_{\text{sh}}$ .

## 4. Summary

Hyperspectral PL imaging followed by comprehensive data analysis allows easy and fast access to the spatial distribution of various opto-electronic and solar cell parameters, such as QFLS, PLQL, ODF, Urbach energy, and shunt resistances of solar cells without the need of specific electrical measurements.

This methodology was adapted and applied here to investigate PSCs patterned with ns and ps laser pulses. Particular attention was paid to the study of the role of the P3 step, investigating the influence of laser impact on the perovskite layer, especially at the scribe-line edges and the areas close to the laser lines. In this way, the effects of ps and ns laser pulses on laser patterning were revealed and an understanding of the nature and extent of material modifications was obtained. Accordingly, both ps and ns laser pulses can be used for successful series interconnection with low power and resistance losses in the very narrow edge regions.

Thus, undesirable material modifications that may occur during laser patterning for series interconnection can be identified and avoided and a comprehensive and detailed picture of the influence of the laser impact on the material properties and thus on the electrical properties of the interconnected cells is obtained.

Our work shows that this approach is able to identify and avoid undesirable material changes that can occur during laser patterning for series interconnection. Moreover, a comprehensive and detailed picture of the influence of laser exposure on opto-electronic material properties and thus on the electrical properties of the interconnected cells is obtained. It has also been demonstrated that the wide range of applications of hyperspectral PL in material characterization is further extended by its beneficial use in process optimization in laser patterning of laser-based electrical series-interconnection, that is now applied to the analysis of laser-based interconnection of perovskite-CIGSe tandem solar cells.<sup>[50]</sup>

## Supporting Information

Supporting Information is available from the Wiley Online Library or from the author.

## Acknowledgements

C.S. and M.F. contributed equally to this work. This work was supported by HTW Berlin (project “LasTa”). Experimental support from the PVcomB and HZB (EE-IS) teams is also acknowledged. Moreover, the authors thank S. Siebentritt (University of Luxembourg) for fruitful discussions.

Open Access funding enabled and organized by Projekt DEAL.

## Conflict of Interest

The authors declare no conflicts of interests.

## Data Availability Statement

The data that support the findings of this study are available from the corresponding author upon reasonable request.

## Keywords

ablation, hyperspectral photoluminescence, lasers, perovskites, photovoltaics, solar modules, thin films

Received: July 13, 2023

Revised: August 31, 2023

Published online: September 24, 2023

- [1] J. S. Manser, J. A. Christians, P. V. Kamat, *Chem. Rev.* **2016**, *116*, 12956.
- [2] G.-W. Kim, A. Petrozza, *Adv. Mater.* **2020**, *10*, 2001959.
- [3] M. A. Green, E. D. Dunlop, G. Siefert, M. Yoshita, N. Kopidakis, K. Bothe, X. Hao, *Prog. Photovolt.* **2023**, *31*, 3.
- [4] J. Li, J. Dagar, O. Shargaieva, M. A. Flatken, H. Köbler, M. Fenske, C. Schultz, B. Stegemann, J. Just, D. M. Töbrens, A. Abate, R. Munir, E. Unger, *Adv. Mater.* **2021**, *11*, 2003460.
- [5] C. Schultz, M. Fenske, J. Dagar, A. Zeiser, A. Bartelt, R. Schlatmann, E. L. Unger, B. Stegemann, *Sol. Energy* **2020**, *198*, 410.
- [6] M. Fenske, C. Schultz, J. Dagar, F. U. Kosasih, A. Zeiser, C. Junghans, A. Bartelt, C. Ducati, R. Schlatmann, E. L. Unger, B. Stegemann, *Energy Technol.* **2021**, *9*, 2000969.
- [7] L. A. Castriotta, M. Zendejdel, N. Yaghoobi Nia, E. Leonardi, M. Löffler, B. Paci, A. Generosi, B. Rellinghaus, A. Di Carlo, *Adv. Mater.* **2022**, *12*, 2103420.
- [8] D. B. Ritzer, T. Abzieher, A. Basibüyük, T. Feeney, F. Laufer, S. Ternes, B. S. Richards, S. Bergfeld, U. W. Paetzold, *Prog. Photovolt.* **2022**, *30*, 360.
- [9] B. Stegemann, C. Schultz, in *Laser Patterning of Thin Films, Digital Encyclopedia of Applied Physics*, Wiley-VCH Verlag GmbH & Co. KGaA, Weinheim, Germany **2019**, pp. 1–30, <https://doi.org/10.1002/3527600434.eap8302019>.
- [10] G. Mincuzzi, A. L. Palma, A. Di Carlo, T. M. Brown, *ChemElectroChem* **2016**, *3*, 9.
- [11] C. Schultz, F. Schneider, A. Neubauer, A. Bartelt, M. Jošt, B. Rech, R. Schlatmann, S. Albrecht, B. Stegemann, *IEEE J. Photovolt.* **2018**, *8*, 1244.
- [12] F. Matteocci, L. Vesce, F. U. Kosasih, L. A. Castriotta, S. Cacovich, A. L. Palma, G. Divitini, C. Ducati, A. Di Carlo, *ACS Appl. Mater. Interfaces* **2019**, *11*, 25195.
- [13] C. Schultz, M. Fenske, J. Dagar, G. A. Farias Basulto, A. Zeiser, A. Bartelt, C. Junghans, R. Schlatmann, E. Unger, B. Stegemann, *Mater. Today Proc.* **2021**, *53*, 299.
- [14] P. Würfel, S. Finkbeiner, E. Daub, *Appl. Phys. A* **1995**, *60*, 67.
- [15] G. Rey, A. Paduthol, K. Sun, T. Nagle, D. Poplavskyy, V. S. Escalant, M. Melchiorre, S. Siebentritt, M. Abbott, T. Trupke, *IEEE J. Photovolt.* **2020**, *10*, 181.
- [16] S. Siebentritt, T. P. Weiss, M. Sood, M. H. Wolter, A. Lomuscio, O. Ramirez, *J. Phys. Mater.* **2021**, *4*, 042010.
- [17] T. Kirchartz, J. A. Márquez, M. Stolterfoht, T. Unold, *Adv. Mater.* **2020**, *10*, 1904134.
- [18] M. C. Schubert, L. E. Mundt, D. Walter, A. Fell, S. W. Glunz, *Adv. Mater.* **2020**, *10*, 1904001.
- [19] A. D. Bui, N. Mozaffari, T. N. Truong, T. Duong, K. J. Weber, T. P. White, K. R. Catchpole, D. Macdonald, H. T. Nguyen, *Prog. Photovolt.* **2022**, *30*, 1038.
- [20] C. O. Ramírez Quiroz, L.-I. Dion-Bertrand, C. J. Brabec, J. Müller, K. Orgassa, *Engineering* **2020**, *6*, 1395.
- [21] G. El-Hajje, C. Momblona, L. Gil-Escrig, J. Ávila, T. Guillemot, J.-F. Guillemoles, M. Sessolo, H. J. Bolink, L. Lombez, *Energy Environ. Sci.* **2016**, *9*, 2286.
- [22] J. Zikulnig, W. Mühleisen, P. J. Bolt, M. Simor, M. De Biasio, *Solar* **2022**, *2*, 1.
- [23] S. Cacovich, G. Vidon, M. Degani, M. Legrand, L. Gouda, J.-B. Puel, Y. Vaynzof, J.-F. Guillemoles, D. Ory, G. Grancini, *Nat. Commun.* **2022**, *13*, 2868.
- [24] M. H. Wolter, R. Carron, E. Avancini, B. Bissig, T. P. Weiss, S. Nishiwaki, T. Feurer, S. Buecheler, P. Jackson, W. Witte, S. Siebentritt, *Prog. Photovolt.* **2022**, *30*, 702.
- [25] F. Babbe, L. Choubrac, S. Siebentritt, *Sol. RRL* **2018**, *2*, 1800248.
- [26] T. Wang, F. Ehre, T. P. Weiss, B. Veith-Wolf, V. Titova, N. Valle, M. Melchiorre, O. Ramírez, J. Schmidt, S. Siebentritt, *Adv. Mater.* **2022**, *12*, 2202076.
- [27] P. Caprioglio, C. M. Wolff, O. J. Sandberg, A. Armin, B. Rech, S. Albrecht, D. Neher, M. Stolterfoht, *Adv. Mater.* **2020**, *10*, 2000502.
- [28] S. Agarwal, M. Seetharaman, N. K. Kumawat, A. S. Subbiah, S. K. Sarkar, D. Kabra, M. A. G. Namboothiry, P. R. Nair, *J. Phys. Chem. Lett.* **2014**, *5*, 4115.
- [29] Y. Augarten, T. Trupke, M. Lenio, J. Bauer, J. W. Weber, M. Juhl, M. Kasemann, O. Breitenstein, *Prog. Photovolt.* **2013**, *21*, 933.
- [30] J. Dagar, K. Hirslandt, A. Merdasa, A. Czudek, R. Munir, F. Zu, N. Koch, T. Dittrich, E. L. Unger, *Sol. RRL* **2019**, *3*, 1900088.
- [31] E. H. Anaraki, A. Kermanpur, L. Steier, K. Domanski, T. Matsui, W. Tress, M. Saliba, A. Abate, M. Grätzel, A. Hagfeldt, J.-P. Correa-Baena, *Energy Environ. Sci.* **2016**, *9*, 3128.
- [32] L. Kegelmann, C. M. Wolff, C. A. Omondi, F. Lang, E. L. Unger, L. Korte, T. Dittrich, D. Neher, B. Rech, S. Albrecht, *ACS Appl. Mater. Interfaces* **2023**, *8*, 3221.
- [33] J. M. Liu, *Opt. Lett.* **1982**, *7*, 196.
- [34] C. Schultz, A. Bartelt, C. Junghans, W. Becker, R. Schlatmann, B. Stegemann, *Appl. Surf. Sci.* **2021**, *536*, 147721.
- [35] E. V. Péan, S. Dimitrov, C. S. De Castro, M. L. Davies, *Phys. Chem. Chem. Phys.* **2020**, *22*, 28345.
- [36] A. Compaan, I. Matulionis, S. Nakade, Optimization of Laser Scribing for Thin-Film PV Modules. Final Technical Progress Report, Final Technical Progress Report, The University of Toledo Toledo, OH **1998**, p. 43.
- [37] A. Delamarre, L. Lombez, J.-F. Guillemoles, *J. Photon. Energy* **2012**, *2*, 027004.
- [38] C. Schultz, Ph.D. Thesis, Technische Universität Berlin, **2021**, pp. 1–246.
- [39] M. Sood, A. Urbaniak, C. Kameni Boumenou, T. P. Weiss, H. Elanzeery, F. Babbe, F. Werner, M. Melchiorre, S. Siebentritt, *Prog. Photovolt.* **2022**, *30*, 263.
- [40] C. Kaiser, O. J. Sandberg, N. Zarrabi, W. Li, P. Meredith, A. Armin, *Nat. Commun.* **2021**, *12*, 3988.
- [41] M. Ledinsky, T. Schönfeldová, J. Holovský, E. Aydin, Z. Hájková, L. Landová, N. Neyková, A. Fejfar, S. De Wolf, *J. Phys. Chem. Lett.* **2019**, *10*, 1368.
- [42] E. Ugur, M. Ledinsky, T. G. Allen, J. Holovský, A. Vlk, S. De Wolf, *J. Phys. Chem. Lett.* **2022**, *13*, 7702.
- [43] J. Chantana, Y. Kawano, T. Nishimura, A. Mavlonov, T. Minemoto, *Sol. Energy Mater. Sol. Cells* **2020**, *210*, 110502.
- [44] J. Holovský, K. Ridžoňová, A. Peter Amalathas, B. Conrad, R. K. Sharma, X. Y. Chin, E. Bastola, K. Bhandari, R. J. Ellingson, S. De Wolf, *ACS Energy Lett.* **2023**, *8*, 3221.
- [45] L. M. Pazos-Outón, M. Szumilo, R. Lamboll, J. M. Richter, M. Crespo-Quesada, M. Abdi-Jalebi, H. J. Beeson, M. Vrućinić, M. Alsari, H. J. Snaith, B. Ehrler, R. H. Friend, F. Deschler, *Science* **2016**, *351*, 1430.
- [46] T. Kirchartz, F. Staub, U. Rau, *ACS Energy Lett.* **2016**, *1*, 731.

- [47] T. Trupke, R. A. Bardos, M. D. Abbott, J. E. Cotter, *Appl. Phys. Lett.* **2005**, *87*, 093503.
- [48] D. Walter, Y. Wu, T. Duong, J. Peng, L. Jiang, K. C. Fong, K. Weber, *Adv. Mater.* **2018**, *8*, 1701522.
- [49] E. T. Hoke, D. J. Slotcavage, E. R. Dohner, A. R. Bowring, H. I. Karunadasa, M. D. McGehee, *Chem. Sci.* **2015**, *6*, 613.
- [50] C. Schultz, G. A. Farias Basulto, N. Otto, J. Dagar, A. Bartelt, R. Schlatmann, E. Unger, B. Stegemann, *EPJ Photovolt.* **2023**, *14*, 16.